Environmental Science: Atmospheres

ROYAL SOCIETY OF CHEMISTRY

PAPER

View Article Online
View Journal

Cite this: DOI: 10.1039/d5ea00169b

Airborne measurements of peroxyacetyl nitric anhydride (PAN) and peroxyacetic acid (PAA) over the Amazon rainforest: the role of isoprene and the fate of the peroxyacetyl radical

Carolina Nelson, Matthias Kohl, * Sergey Gromov, Andrea Pozzer, Simone T. Andersen, Raphael Dörich, Jos Lelieveld and John N. Crowley *

PAN ($CH_3C(O)O_2NO_2$) and PAA ($CH_3C(O)OOH$) are formed in the atmosphere uniquely and competitively from the same precursor radical ($CH_3C(O)O_2$), whereby the relative rates of formation of PAN and PAA are determined by the abundances of HO_2 and NO_2. Here, we present airborne measurements of PAN and PAA in an altitude range from 0.3–15 km over the Amazon rainforest during the CAFE Brazil campaign, which took place from December 2022 to January 2023. Median PAA mixing ratios (*ca.* 340 pptv) across all analysed flights exceed those of PAN (*ca.* 65 pptv) by more than a factor of 5 in the mid troposphere around 6 km altitude, underlining the dominance of HO_2 over NO_2 chemistry under low NO_X conditions of the Amazon rainforest. Within experimental uncertainty, the median vertical profiles of PAA and PAN throughout the entire measurement campaign are reproduced by the EMAC global chemical transport model. The EMAC analysis reveals that the oxidation of isoprene (emitted from the rainforest) is the primary source of the $CH_3C(O)O_2$ radical. With an average contribution of ~31%, the main direct precursor of $CH_3C(O)O_2$ is methylglyoxal ($CH_3C(O)CHO$), followed by acetaldehyde (17%) and methyl vinyl ketone (10%). At altitudes between 12 and 14 km, only a few percent (<5%) of $CH_3C(O)O_2$ radicals formed result in the production of PAN and PAA. The dominant sink of $CH_3C(O)O_2$ in the upper troposphere is NO, while at lower altitudes, its reaction with other organic peroxy radicals produces acetic acid and CH_3O_2. The CH_3O_2 production resulting (*via* reactions of $CH_3C(O)O_2$) from isoprene oxidation over the Amazon rainforest contributes between 9 and 44% to total CH_3O_2 production and surpasses the contribution from methane oxidation at altitudes below 4 km. Through the formation of $CH_3C(O)O_2$, isoprene oxidation in this region thus significantly influences not only PAN and PAA formation but also the yields of acetic acid as well as methylperoxynitrate, methylhydroperoxide and formaldehyde, which are products of CH_3O_2 reactions with HO_2 and NO, and photochemical precursors to HO_x.

Received 16th December 2025
Accepted 17th March 2026

DOI: 10.1039/d5ea00169b

rsc.li/esatmospheres

Environmental significance

Emissions from the Amazon rainforest have a substantial environmental impact, both on regional and global scales. We show that the chemistry around the peroxyacetyl radical in the air above the rainforest is dominated by biogenic emissions of isoprene, the oxidation of which represents the major source of organic trace gases required to generate peroxyacetyl nitric anhydride (PAN). PAN is a centrally important atmospheric reservoir of reactive nitrogen, which is closely linked to tropospheric ozone formation. In addition, isoprene oxidation is a major source of peroxides, especially peracetic acid, with a significant contribution to methyl hydoperoxide production.

1 Introduction

Peroxyacetyl nitric anhydride ($CH_3C(O)O_2NO_2$, also known as peroxyacetyl nitrate and commonly abbreviated as PAN) and peroxyacetic acid ($CH_3C(O)OOH$, PAA) are important tropospheric trace gases whose atmospheric distribution is governed by a complex interplay of chemical and physical processes. Both PAN and PAA are formed in volatile organic compound (VOC)-fuelled and NO-catalysed chemical cycles, which drive tropospheric ozone (O_3) formation.

The significance of PAN in the atmosphere and its impact on human health have been recognized for decades.[1–3] PAN plays a central role in the chemistry of the troposphere on local to global scales, as it is the principal tropospheric reservoir species of NO_X in many regions, especially above the boundary layer.[3–5] As PAN is thermally labile, its lifetime in the temperate boundary layer is only a few hours, but in the middle to upper troposphere at temperatures between −10 and −50 °C, PAN has

Atmospheric Chemistry Department, Max-Planck-Institute for Chemistry, 55128-Mainz, Germany. E-mail: john.crowley@mpic.de; m.kohl@mpic.de

a lifetime of weeks to months with respect to thermal decomposition. This enables PAN to sequester NO_2 from polluted areas, transport it over long distances around the globe, and release it to pristine regions when air masses descend and warm.

PAA is a ubiquitous atmospheric organic hydroperoxide (ROOH), second only in concentration to CH_3OOH, with mixing ratios reaching up to 1 ppbv in urban and rural areas[6–8] and tens to hundreds of pptv in the upper troposphere (UT).[9,10] It can serve as a reservoir of HO_2, which in turn impacts gas-phase oxidation rates and the radical budget.[11] Due to its high solubility, PAA may play a potentially important role in SOA formation, and it oxidises sulphur (IV) at atmospheric pH levels.[12] PAA is also an organic acid, and as such, it contributes to the acidity of the atmosphere, which has impacts on air quality and acid deposition.[13,14]

The Amazon rainforest, the largest global source of volatile organic compounds (VOCs),[15] has a profound impact on regional weather and climate in the tropics and globally. However, the impact of specific non-methane volatile organic compounds (NMVOCs), particularly isoprene, lightning-NO_X and biomass burning on PAN production, is not well quantified.[16] Aircraft measurements of PAN over Amazonia are sparse, with only a few studies available.[17–19] Measurements of PAA are even less common in this region. Yet, these kinds of measurements are needed to answer open questions such as the role of PAN as a source of NO_X in remote areas and hence its impact on O_3 chemistry.

The Amazonian region is susceptible to climate change and threatened by deforestation,[20,21] which further complicates the prediction of future PAN and PAA levels and distributions.

Although they have very different physio-chemical properties, PAN and PAA are closely linked as they are competitively formed in the atmosphere from the same precursor, the peroxyacetyl radical ($CH_3C(O)O_2$). Fig. 1 depicts the most important production and loss reactions of the $CH_3C(O)O_2$ radical, which define PAN and PAA formation in the atmosphere.

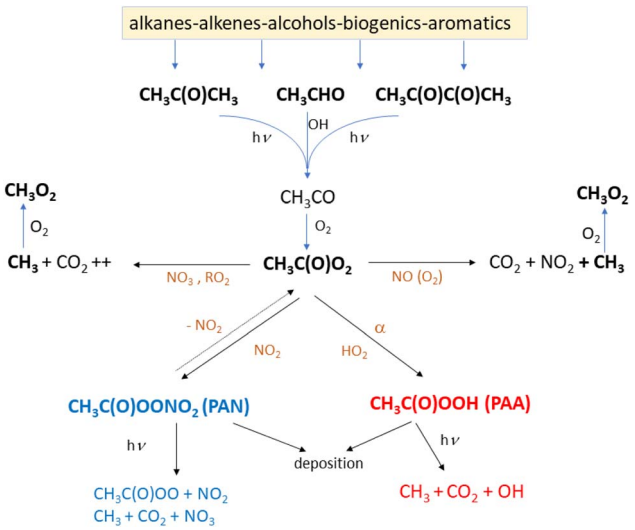

Fig. 1 Pathways to $CH_3C(O)O_2$ production from organic precursors and its further reactions forming PAN (blue) and PAA (red), as well as CH_3O_2.

On a global scale, the major direct $CH_3C(O)O_2$ precursor reactions are the OH-initiated oxidation of acetaldehyde and the photolysis of acetone and methyl glyoxal (MGLY; $CH_3C(O)CHO$),[22] all of which result in the formation of the CH_3CO radical, which is quasi instantaneously converted to $CH_3C(O)O_2$ *via* reaction with O_2 (R1). Depending on temperature and pressure, between 2 and 8% of the reaction proceeds *via* a bimolecular channel to form OH and a cyclic lactone that decomposes to HCHO and CO (R2).[23,24]

$$CH_3CO + O_2 + M \rightarrow CH_3C(O)O_2 + M \quad (R1)$$

$$CH_3CO + O_2 \rightarrow OH + HCHO + CO \quad (R2)$$

As shown in Fig. 1, the reaction of $CH_3C(O)O_2$ with NO_2 leads to the formation of PAN (R3), which can thermally decompose back to the reactants (R4) and is also lost *via* photolysis to reform $CH_3C(O)O_2$ (R5a) or CH_3CO_2 (R5b).

$$CH_3C(O)O_2 + NO_2 + M \rightarrow CH_3C(O)O_2NO_2\ (PAN) + M \quad (R3)$$

$$CH_3C(O)O_2NO_2\ (PAN) + M \rightarrow CH_3C(O)O_2 + NO_2 + M \quad (R4)$$

$$CH_3C(O)O_2NO_2\ (PAN) + h\nu \rightarrow CH_3C(O)O_2 + NO_2 \quad (R5a)$$

$$CH_3C(O)O_2NO_2\ (PAN) + h\nu \rightarrow CH_3CO_2 + NO_3 \quad (R5b)$$

CH_3CO_2, which is also formed in the reaction of $CH_3C(O)O_2$ with NO (R6), is unstable and (in the presence of O_2) forms $CH_3O_2 + CO_2$ (R7).

$$CH_3C(O)O_2 + NO \rightarrow CH_3CO_2 + NO_2 \quad (R6)$$

$$CH_3CO_2 + M\ (+O_2) \rightarrow CH_3O_2 + CO_2 + M \quad (R7)$$

The $CH_3C(O)O_2$ radical can also react with HO_2 (R8) to form PAA (R8a) and other products:

$$CH_3C(O)O_2 + HO_2 \rightarrow CH_3C(O)OOH\ (PAA) + O_2 \quad (R8a)$$

$$CH_3C(O)O_2 + HO_2 \rightarrow CH_3C(O)OH + O_3 \quad (R8b)$$

$$CH_3C(O)O_2 + HO_2 \rightarrow CH_3CO_2 + O_2 + OH \quad (R8c)$$

According to IUPAC's temperature-dependent parameterisation of the branching ratio, (R8a)–(R8c) account for 37%, 13% and 50% of the reaction, respectively, at room temperature. At a temperature of −50 °C (*e.g.* as in the upper troposphere), the fractional contributions are 26%, 47% and 27%.[25] $CH_3C(O)O_2$ can also react with other organic peroxy radicals (RO_2) (R9) and NO_3 (R10):

$$CH_3C(O)O_2 + RO_2 \rightarrow CH_3CO_2 + RO + O_2 \quad (R9)$$

$$CH_3C(O)O_2 + NO_3 \rightarrow CH_3CO_2 + NO_2 + O_2 \quad (R10)$$

where RO represents an organic alkoxy radical.

The rate coefficient for the reaction of PAA with OH is very slow, and above the boundary layer, where deposition will play a role,[6] the most significant tropospheric loss process for PAA is its photolysis (R11),[9,26] with a small contribution from reaction with OH (R12).

$$CH_3C(O)OOH + h\nu \rightarrow CH_3CO_2 + OH \quad (R11)$$

$$CH_3C(O)OOH + OH \rightarrow CH_3C(O)O_2 + H_2O \quad (R12)$$

From the set of reactions above, we see that not only PAN and PAA are formed from reactions of the $CH_3C(O)O_2$ radical, but *via* several different pathways ((R5b), (R6), (R8c), (R9), (R10) and (R11)), also the CH_3CO_2 radical and thus (*via* (R7)) the methylperoxy radical (CH_3O_2) are formed.

Since both PAN and PAA are uniquely formed *via* the $CH_3C(O)O_2$ radical,[27] their overall production rates depend on the abundance of NO_2 and HO_2 relative to the other reactants and the ratio of PAN to PAA serves as an indication of the ratio of NO_2 and HO_2 during their photochemical generation.[6,28]

The fraction of the $CH_3C(O)O_2$ radical that reacts to form PAN (f) or PAA (g) is given by:

$$f = k_3[NO_2]/(k_3[NO_2] + k_8[HO_2] + k_6[NO] + k_9[RO_2] + k_{10}[NO_3]) \quad (1)$$

$$g = k_{8a}[HO_2]/(k_3[NO_2] + k_8[HO_2] + k_6[NO] + k_9[RO_2] + k_{10}[NO_3]) \quad (2)$$

In these expressions, k_i represents the rate coefficient associated with reaction R_i.

2 The CAFE Brazil campaign

Between 11/20/2022 and 01/29/2023, 16 research flights (RF05–RF20) were performed over the Amazon rainforest as part of the CAFE Brazil measurement campaign (Chemistry of the Atmosphere: Field Experiment in Brazil), which was based at Manaus Airport, Brazil (3.03 °S, 60.04 °W, UTC-4 hours). An overview of all research flights has been published by Curtius *et al.*[29]

PAN and PAA were measured during 12 research flights (RF05–RF07, RF10, RF11, RF13–RF18 and RF20) with 90% data coverage. The flight tracks (presented in Fig. 2 and S1) covered a geographical extent from approximately 75 °W to 47 °W and 12 °S to 5 °N, as well as an altitude range of approximately 300–14 000 m, resulting in a total flight distance of almost 70 000 km.

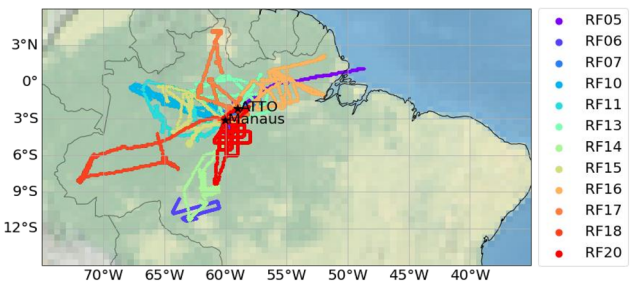

Fig. 2 Flight tracks where PAN and PAA were measured during the CAFE Brazil campaign and included in this analysis.

2.1 Flight tracks and regions covered

As depicted in Fig. 2, the research flights targeted continental regions almost exclusively. The research flights RF06 and RF14 towards the far south of Manaus targeted deforested areas, in contrast to the intact rainforest surrounding Manaus. The flight patterns also included late-evening and nocturnal flights (RF13, RF16, and RF18) and early-morning flights (RF15, RF17, and RF20) to cover nighttime chemistry and particle formation after sunrise. Most data were captured at altitudes between 9 and 15 km, with a focus on sampling outflow from convective systems. Some flights were also dedicated to sampling the tropical forest boundary layer (RF15) and performing vertical profiling (RF05, RF07, and RF18).

The CAFE Brazil campaign took place during the transition phase from the dry to wet season and hence outside the peak biomass burning season in southern America and southern Africa. Satellite observations indicate that fire activity in Amazonia during CAFE Brazil was generally low and decreased over the course of the campaign as the transition from dry to wet season progressed. Fig. S2 in the SI depicts the open fires detected with >95% confidence by the MODIS instrument mounted on the Terra and Aqua satellites and provided by the NASA FIRMS tool during the CAFE Brazil campaign and shows that most of the fire events in Brazil took place along the northeast coast at the beginning of the campaign.

2.2 Meteorological conditions and back trajectories

During the first half of the campaign in December, the conditions were still relatively dry and hot, while in January, rain events became more frequent. Basic meteorological parameters (including wind speed and direction, temperature and pressure) were recorded during the flights by the BAHAMAS instrument onboard the HALO aircraft[30] and provided by the German Aerospace Center (DLR). As depicted in Fig. S3, the predominant wind direction at all heights during the January flights was from the southeast, indicating a continental origin of the sampled air masses. In December, the wind direction ranged from northeast to southeast. In addition, high wind speeds between 25 and 30 m s^{-1} were slightly less frequent during December than during January.

Ten-day back-trajectories depicting the origin of the air sampled along the flight tracks were calculated at 1-minute intervals using HYSPLIT (Version 5.2;[31]) with one-degree archived meteorological data from the Global Data Assimilation System (GDAS). As shown in Fig. 3, the origin of the air masses sampled during CAFE Brazil depended heavily on altitude. With few exceptions, trajectories starting at mid (8–11 km, yellow) and high altitudes (>12 km, red) were confined to the continent, suggesting that the impact of long-range transport on the observed PAN and PAA levels in the mid and upper troposphere was likely low. In contrast, most low-altitude trajectories (<3 km, green) originated from the central Atlantic

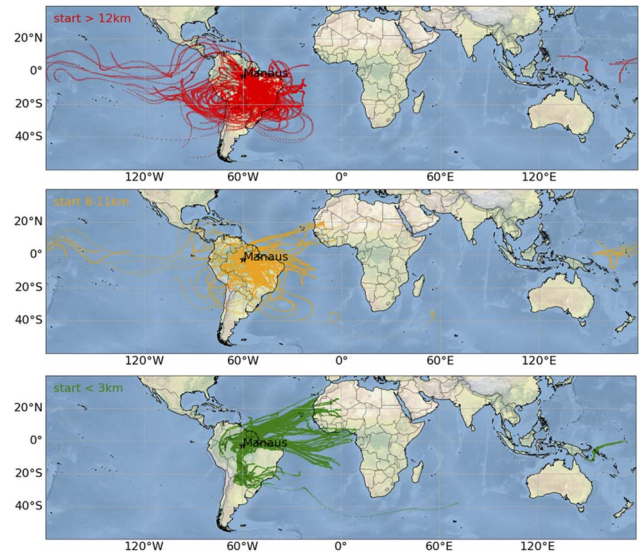

Fig. 3 Ten-day backward trajectories of air masses sampled during CAFE Brazil, calculated with HYSPLIT for every ten minutes along the flight tracks. The panels are separated by the altitude of the starting point along the flight track: low altitudes (green, <3 km, bottom panel), mid altitudes (orange, 8–11 km, middle panel), and high altitudes (red >12 km, upper panel).

and West Africa, and passed over the north-west coast of Brazil, where satellite observations recorded biomass burning events. Hence, the PAN and PAA measurements at low altitudes could be impacted by urban pollution and/or biomass burning from source regions in South America or West Africa.

3 Methods

The CAFE Brazil campaign was conducted using the High Altitude and Long-Range Research aircraft (HALO, Gulfstream G550) as the platform for an instrument payload similar to that deployed on previous CAFE campaigns.[32] Here we focus on the PAN and PAA data obtained using an iodide-chemical ionisation mass spectrometer (CIMS).

3.1 Iodide-chemical ionisation mass spectrometer (CIMS)

The measurement principle of the CIMS instrument is based on the thermal dissociation of PAN to the peroxy radical ($CH_3C(O)O_2$), which reacts with iodide to form the acetate anion ($CH_3CO_2^-$), detected at m/z 59.[33,34] PAA is also detected *via* its conversion to the acetate anion subsequent to reaction with I^-.

The instrument details, its ion-source and its configuration during aircraft measurements have been described elsewhere.[7,9,35,36] For the CAFE Brazil campaign, the primary iodide ions were generated using photo-ionisation of CH_3I[37] rather than an electrical discharge[36] or α particles emitted by ^{210}Po,[35] as on previous missions. The photo-electron generated by irradiation of CH_3I at ~120 nm attaches to CH_3I to form I^-. As both PAN and PAA are detected as the same anion at m/z 59, the periodic titration (once every 150 s with a duty cycle of 50% for each trace gas) of $CH_3C(O)O_2$ in the heated thermal-dissociation inlet was used to differentiate between the two molecules.

PAN was calibrated hourly, in flight, using a photo-chemical PAN source based on the photolysis of acetone in the presence of known amount of NO.[38,39] In the calibration source, acetone in air is photolysed at ~285 nm to generate $CH_3C(O)O_2$ and CH_3O_2 radicals that progressively oxidize NO to NO_2, 90 ± 5% of which forms PAN. The calibration was performed by adding PAN to air that had been zeroed by passing it over steel wool at 140 °C, which removes *e.g.* acids and nitrates without affecting the mixing ratio of H_2O. The total measurement uncertainty for PAN is estimated as 30% as described in the SI.

The instrument sensitivity for PAA was derived once during the campaign (on the ground) using a $CH_3C(O)OOH$ diffusion source, which was sampled by both the CIMS and a modified commercial instrument for total organic peroxides (HYPHOP, see ref. 9 for details), and assigned an uncertainty of a factor two, as described in the SI. In addition, PAA data were corrected for the humidity dependence of its sensitivity, which was derived post-campaign in laboratory experiments (for details see the SI).

The instrumental background signal (usually <6 counts) on m/z = 59 was derived for each flight after landing, when the instrument was flushed with pure nitrogen. This was used to derive the limits of detection (LODs) for PAA of 14–98 pptv (3σ). The LOD (3σ) of PAN was derived from the variability of the PAA titration signal (20–59 pptv).

3.2 Global chemistry transport model (EMAC)

The EMAC model couples the Modular Earth Submodel System (MESSy2)[40,41] to the ECHAM5 (ref. 42) general circulation model. Simulations use a horizontal resolution of 1.875° × 1.875° with 31 layers up to 10 hPa (22 layers in the troposphere), and a time step of 7.5 minutes. The chemistry scheme implemented in EMAC is the Mainz Organic Mechanism (MOM),[43] comprising about 600 species and 1600 reactions, and including a large selection of organic precursors, including isoprene. We adopt the setup of Pozzer *et al.*[44] with the following updates: gas phase rate coefficients related to PAN and PAA formation and loss follow the latest IUPAC recommendations,[25] anthropogenic emissions are taken from the CEDS inventory[45] and biomass and agricultural waste burning emissions follow Andreae,[46] based on fire type and observed dry matter burnt.[47] Biogenic emissions are calculated online using the Model of Emissions of Gases and Aerosols from Nature (MEGAN[48]) and lightning NO_X is parameterized following Grewe.[49] Total production and loss rates of relevant species, as well as key individual reaction rates, are diagnosed online. All model data presented were sampled along the CAFE Brazil flight tracks corresponding to time steps by the submodel S4D.[50]

4 Results and discussion

The flights included in the analysis are listed in Table 1 and the corresponding flight tracks depicted in Fig. 2. Details of measured PAN and PAA along all flight tracks are given in Fig. S1 and S4 in the SI. Limits of detection (LODs) and measured mixing ratios are given in parts per trillion per

Table 1 Overview of flights during the CAFE Brazil campaign when PAN and PAA were measured[a]

Flight	Take-off (UTC)	Landing (UTC)	PAN min-max (LOD)[a]	PAA min-max (LOD)[a]
RF05	22-12-04 12:30	22-12-04 20:30	0–300 (36)	200–800 (17)
RF06	22-12-07 14:20	22-12-07 22:50	0–250 (36)	50–800 (18)
RF07	22-12-09 15:20	22-12-10 10:00	0–300 (33)	100–1150 (98)
RF10	22-12-16 16:05	22-12-17 00:30	0–300 (59)	100–900 (14)
RF11	22-12-19 14:33	22-12-19 21:57	0–200 (45)	200–1000 (33)
RF13	23-01-08 20:20	23-01-09 05:30	0–100 (30)	200–500 (19)
RF14	23-01-12 13:50	23-01-12 22:10	0–150 (33)	100–550 (27)
RF15	23-01-14 11:49	23-01-04 20:48	0–150 (24)	50–350 (28)
RF16	23-01-17 03:40	23-01-17 12:39	0–120 (26)	100–300 (27)
RF17	23-01-18 12:17	23-01-18 21:43	0–120 (20)	50–350 (18)
RF18	23-01-21 19:25	23-01-22 04:01	0–200 (26)	100–750 (28)
RF20	23-01-26 08:48	23-01-26 18:38	50–150 (29)	150–450 (50)

[a] Approx. min and max values are given in pptv. The LOD (in pptv) is defined as 3σ background.

volume or parts per billion per volume, which are further referred to as pptv and ppbv, respectively. The variation in the LOD for PAN is related to atmospheric variability and size of the PAA signal (an interpolated value of which has to be subtracted from the sum-signal to derive PAN mixing ratios). The occasionally poor LOD for PAA (*e.g.* flights RF07 and RF20) is due to a large difference in the background signals at m/z 59 when comparing the two pre-flight and post-flight zero values.

4.1 Vertical profiles of PAN and PAA and the PAN-to-PAA ratio

Fig. 4 shows the vertical distribution of the measured (CIMS) and modelled (EMAC) PAN and PAA mixing ratios, where the median values per altitude bin (1 km) are shown as large data points connected with a solid line.

The PAN mixing ratios range from below the detection limit (most frequently encountered in the boundary layer) to maxima of ~370 pptv detected in single plumes. The median PAN mixing ratio exhibits a mid-tropospheric maximum of ~100 pptv at about 8 km altitude, above which it decreases slowly with increasing altitude to ~70 pptv at ~14.5 km. At these altitudes, in the absence of long-range transport from PAN-rich regions (see Fig. 3), the presence of PAN in the upper troposphere is likely due to *in situ* production resulting from convectively uplifted VOCs and lightning NO_x evidence for which is presented in Curtius *et al.*[29] The EMAC simulations reproduce the low PAN mixing ratios accurately up to about 3 km, above which the simulated mixing ratios are lower than the measurements by 30–40%. The model reproduces the flattening of the vertical profile above 9 km and the non-zero mixing ratios at altitudes as high as 14.5 km.

With median 1 km-altitude-binned mixing ratios up to almost 400 pptv, the PAA mixing ratios over the Amazon rainforest are clearly much higher than those of PAN (by about a factor of 20 at low altitudes, a factor of 5 at mid altitudes and factor of 2 at high altitudes), which reflects the enhanced rate of reaction of $CH_3C(O)O_2$ with HO_2 compared to NO_2 in this low-NO_X environment. The vertical profile of PAA shows a maximum around 2 km with a quasi-monotonic decrease from 2 km to 14 km and lower values in the boundary layer, presumably due to deposition-related loss of PAA and the organic precursors.

As for PAN, the EMAC simulation reproduces the median vertical profile of PAA within the measurement uncertainty, with the largest deviation at ~7 km (1.5-fold model overestimation).

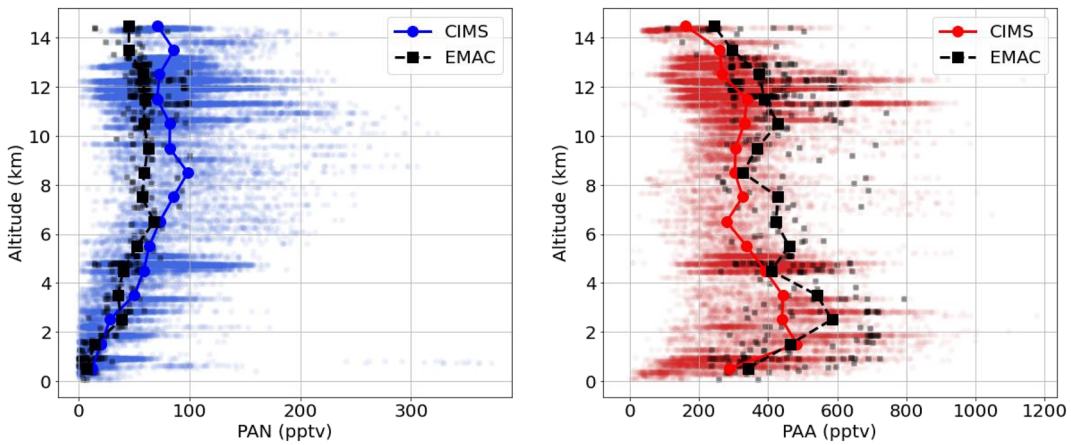

Fig. 4 Measured (CIMS) and modelled (EMAC) mixing ratios of PAN (left panel) and PAA (right panel) during CAFE Brazil. The median for each altitude bin (1 km) is marked by large symbols connected by a line.

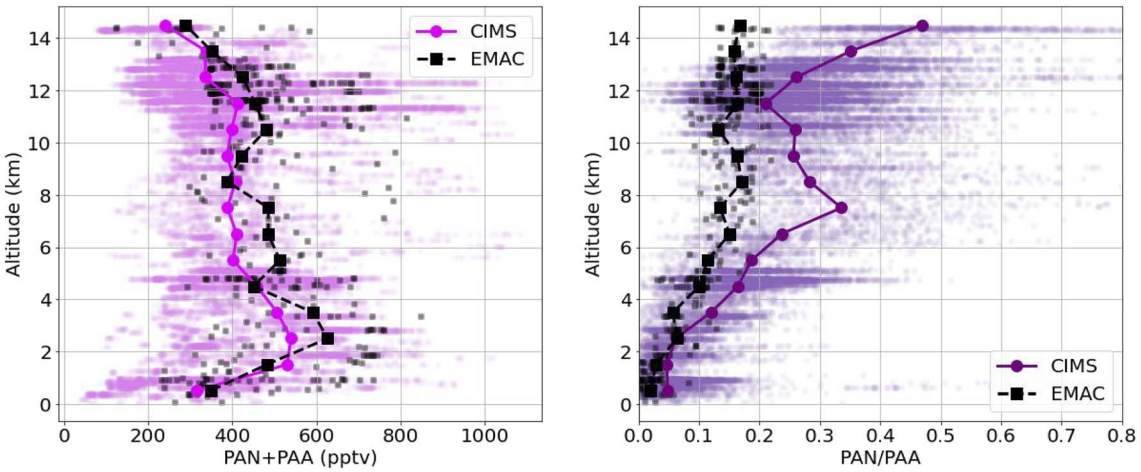

Fig. 5 Measured (CIMS) and modelled (EMAC) sum of PAN + PAA (left panel) and ratio of PAN/PAA (right panel) during the CAFE Brazil campaign. The median for each altitude bin (1 km) is marked by large symbols connected by a line.

The largest deviations between the EMAC simulation and the measurements are found in the mid and upper troposphere for PAN and in the mid and lower troposphere for PAA. As we show later, these are the regions where the respective *in situ* production rate is expected to be highest and may indicate that discrepancies between the model and measurements in these altitude regions are associated with bias in the chemical production mechanisms rather than in the loss terms.

By summing the mixing ratios of PAN and PAA and comparing them with the EMAC simulation, we can examine how well the model captures the fate of the $CH_3C(O)O_2$ radical with respect to reactions with NO_2 and HO_2 (to form PAN and PAA, respectively) or with NO and other RO_2. In the left panel of Fig. 5, we plot the measured (CIMS) and simulated (EMAC) sum of PAN and PAA.

Good agreement (deviations of up to 20%) is observed between the measured and simulated median vertical profiles of PAN + PAA. This does not necessarily imply that the modelled $CH_3C(O)O_2$ levels are correct, as the sum of PAN and PAA is determined by both the total production rate of $CH_3C(O)O_2$ and its fractional reaction with HO_2 and NO_2 (in competition with RO_2 and NO).

When plotting the simulated and measured PAN/PAA ratio (right panel in Fig. 5), we see greater model–measurement deviations, close to a factor of two overestimation by EMAC at 7–8 km and 14 km. The PAN-to-PAA ratio is controlled by both the relative rate of reaction of the $CH_3C(O)O_2$ radical with NO_2 and HO_2, respectively, and the relative loss frequencies of PAN and PAA. The loss term of PAA is dependent mainly on its photolysis frequency, for which measured and simulated values are in good agreement (see Fig. S5 in the SI), and at altitudes above 5 km where the lifetime of PAN is dominated by photolysis, the same applies. The model–measurement deviation is thus most likely driven by a positive bias in the simulated HO_2/NO_2 ratio.

The overall model (numerical) uncertainty depends on the errors in emissions, transport and photochemical processes, which are different for each gas species and location. An important contribution to the uncertainty associated with the simulation of PAN is the model accuracy in reproducing NOx. As shown by Nussbaumer *et al.*,[51] the model shows very good agreement with the observations, reproducing the vertical profile of the observations, with median values that agree within 20% along the entire troposphere. In the absence of HO_2 measurememts (unavailable owing to ongoing calibration concerns) and NO_2 measurements (available only as estimates based on measurements of NO, J-NO_2 and O_3), we cannot test the hypothesis that the model–measurement deviation is driven by a positive bias in the simulated HO_2/NO_2 ratio. The (possible) model HO_2/NO_2 bias will be revisited in a future publication exploring the coupling of the HO_X and NO_X chemical cycles when HO_X data become available.

4.2 Sources and sinks of the $CH_3C(O)O_2$ radical in the EMAC model

As EMAC is able to accurately reproduce the sum of PAA and PAN mixing ratios, we now examine the model sources of $CH_3C(O)O_2$ in detail, initially focusing on the globally most important ones according to Fischer *et al.* (2014), which are acetone ($CH_3C(O)CH_3$), acetaldehyde (CH_3CHO) and methylglyoxal (MGLY; $CH_3C(O)CHO$). The modelled mean vertical profiles for 1-km altitude bins of each of these are depicted in the left panel of Fig. 6.

The modelled mixing ratios of $CH_3C(O)CHO$, acetone and acetaldehyde all decrease with increasing altitude since their primary sources are in the boundary layer. Acetone is longer lived (lifetime ~10 days in the UT and 20 days in the boundary layer[52,53] and is much more abundant than the other two precursors, with mixing ratios reaching up to 1.27 ppbv at low altitudes and 570 pptv at high altitudes. At values close to 100 pptv, the mixing ratios of acetaldehyde and MGLY are similar at around 4 km. MGLY is more abundant than acetaldehyde at lower altitudes and the opposite is true above 4 km. This reflects the differences in loss terms, which are dominated by photolysis for MGLY and by reaction with OH for acetaldehyde.

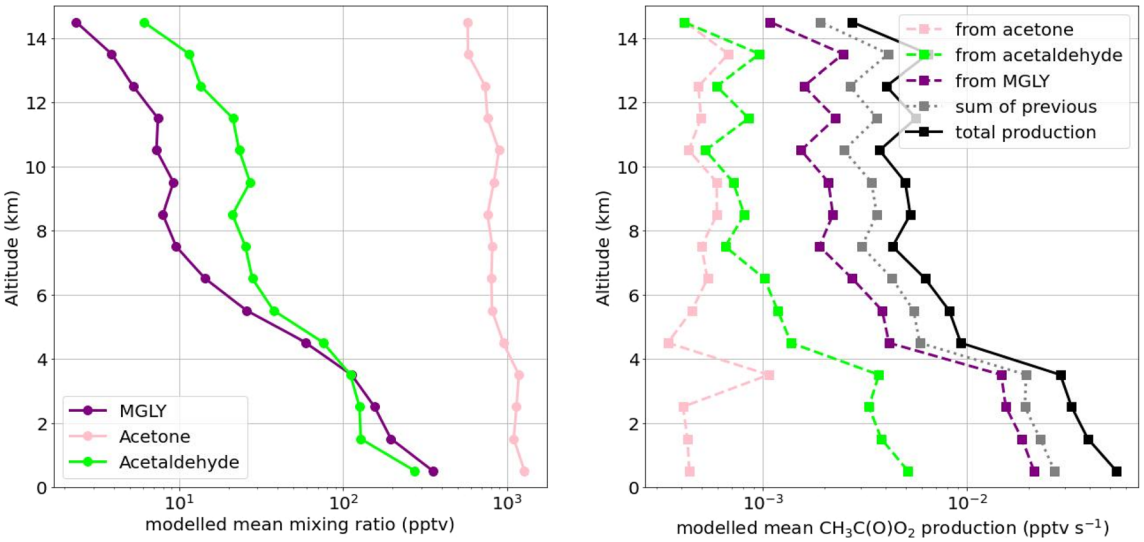

Fig. 6 Left panel: mean vertical profiles of modelled methylglyoxal (purple), acetone (pink) and acetaldehyde (lime) by EMAC during the CAFE Brazil campaign. Right panel: mean vertical profiles of 1 km-altitude bins of modelled $CH_3C(O)O_2$ production from acetone photolysis (pink), acetaldehyde oxidation (lime) and methylglyoxal photolysis and oxidation reactions (purple). The grey line represents the summed contribution of the three depicted precursors, and the black line represents the total model production of $CH_3C(O)O_2$.

In the right panel of Fig. 6, we plot the mean modelled individual production rate of each of acetaldehyde, acetone and $CH_3C(O)CHO$ contributing to $CH_3C(O)O_2$ production retrieved from following reactions in the model, as well as the total production rate from all $CH_3C(O)O_2$-producing reactions included in the EMAC chemical mechanism:

$$CH_3CHO + OH\ (+O_2) \rightarrow CH_3C(O)O_2 + H_2O \quad (R13)$$

$$CH_3C(O)CH_3 + h\nu\ (+2\ O_2) \rightarrow CH_3C(O)O_2 + CH_3O_2 \quad (R14)$$

$$CH_3C(O)CHO + h\nu\ (+2\ O_2) \rightarrow CH_3C(O)O_2 + HO_2 + CO \quad (R15)$$

$$CH_3C(O)CHO + OH\ (+O_2) \rightarrow CH_3C(O)O_2 + CO + H_2O \quad (R16)$$

$$CH_3C(O)CHO + NO_3\ (+O_2) \rightarrow CH_3C(O)O_2 + CO + H_2O \quad (R17)$$

Reactions (R13)–(R17) are composite reactions in which the initially formed CH_3CO radical reacts instantaneously with O_2 to form $CH_3C(O)O_2$ (R1).

The total $CH_3C(O)O_2$ production in the model ranges between 0.003 and 0.05 pptv s^{-1}, with the maximum at the lowest altitudes. The largest single contribution to the $CH_3C(O)O_2$ production rate is from MGLY, which has its maximum value in the lower troposphere <3 km (0.02 pptv s^1). Although all three MGLY degradation terms (R15)–(R17) contribute to $CH_3C(O)O_2$ formation, photolysis (R15) is dominant during the day at all altitudes (68–90%). The second largest contribution to $CH_3C(O)O_2$ formation in the model is from acetaldehyde, which is most important at the lowest altitudes (*ca.* 5×10^{-3} pptv s^1). Above 8 km altitude, the absolute $CH_3C(O)O_2$ production from acetone and acetaldehyde is in a comparable range (around 5×10^{-4} pptv s^1). Compared to MGLY and acetaldehyde the mean absolute contribution from acetone increases slightly with altitude (around 4–7 $\times$ 10^{-4} pptv s^1), which is related to the higher photolysis frequency at higher altitudes. At altitudes lower than 5 km, the photolysis of acetone plays a negligible role compared to the dominant production of $CH_3C(O)O_2$ from MGLY photolysis.

Fig. 7 depicts the average fractional contributions to $CH_3C(O)O_2$ formation along all flight tracks during the CAFE Brazil campaign. The left panel in Fig. 7 shows that the vast majority of $CH_3C(O)O_2$ in the model during CAFE Brazil results from primary production *via* the intermediate precursor CH_3CO radical (90%, blue), while the recycling of $CH_3C(O)O_2$ *via* the thermal decay of PAN only accounts for around 8% (orange) on average over the whole campaign. The remaining fraction "others" (grey, 2%) includes $CH_3C(O)O_2$ production from reactions with single contributions of less than 2%.

In the right panel of Fig. 7, we depict the campaign-averaged contributions of selected, specified CH_3CO precursors. The fraction "others" (grey, 15%) includes the contribution of all unspecified reactions (~8.7%) and reactions with single contributions of less than 2% (~6.6%). Fig. 7 (right panel) highlights the dominant role of the isoprene-oxidation product MGLY in the generation of CH_3CO and hence $CH_3C(O)O_2$ over the Amazon rainforest. MGLY is a second- and third-generation product of isoprene (C_5H_8) oxidation, while global primary sources of MGLY, such as biomass burning (5%), biofuel use (3%) or other anthropogenic emissions (5%), are minor.[54] As the Amazon rainforest is a vast source of biogenic VOCs, with isoprene being the dominant compound emitted from vegetation,[15,55,56] the important role of MGLY in $CH_3C(O)O_2$ production over the Amazon rainforest is readily understood. The large contribution of MGLY is consistent with the global average contribution of around 30%, as reported in ref. 22. As seen in Fig. 7 (right panel), the primary single contribution to CH_3CO production in the model is the photolysis of MGLY (*ca.* 25%). Adding the reaction of MGLY + OH, the isoprene oxidation

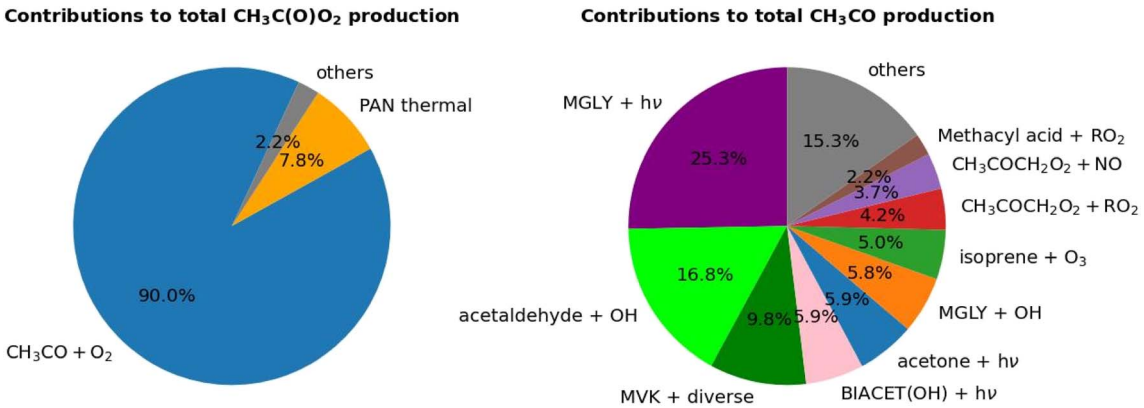

Fig. 7 Percentage contributions of $CH_3C(O)O_2$ production in the model averaged along the flight tracks during the CAFE Brazil campaign (left panel) and identified principle CH_3CO precursors in the model leading to the primary production of $CH_3C(O)O_2$ (right panel).

product MGLY accounts for about 31% of the total model CH_3CO production.

With a contribution of ~17%, the second-largest single contribution to CH_3CO production is the oxidation of acetaldehyde. The sources of acetaldehyde in the model are manifold and can result from both anthropogenic and biogenic sources, among others within the isoprene photooxidation chain. Compared to the global average of 44% estimated by Fischer *et al.*,[22] the acetaldehyde contribution during CAFE Brazil is less than half of this value, highlighting the strong regional variability of $CH_3C(O)O_2$ production mechanisms and the dominance of isoprene chemistry over the Amazon.

Acetone, as a direct precursor to $CH_3C(O)O_2$, accounts for around 6% during CAFE Brazil, which aligns with the global average contribution reported by Fischer *et al.*[22] When its indirect contributions from reactions of its oxidation products $CH_3C(O)CH_2O_2$ + RO_2 (4.2%) and $CH_3C(O)CH_2O_2$ + NO (3.7%) are taken into account, the impact of acetone approximately doubles. However, together, the relative contribution of acetaldehyde and acetone to $CH_3C(O)O_2$ -production during CAFE Brazil over the Amazon rainforest accounts for only about a quarter of the total model $CH_3C(O)O_2$ production.

The total contribution to $CH_3C(O)O_2$ production *via* reactions that are directly or indirectly linked to isoprene (isoprene + O_3, MGLY, BIACET(OH), methylvinylketon (MVK), methacyl acid) sums up to 54%, allowing us to conclude that $CH_3C(O)O_2$ formation over the Amazon rainforest is predominately driven by the oxidation of isoprene.

Note that during CAFE Brazil, the highest data coverage was at high altitudes and during daytime; therefore, the average over

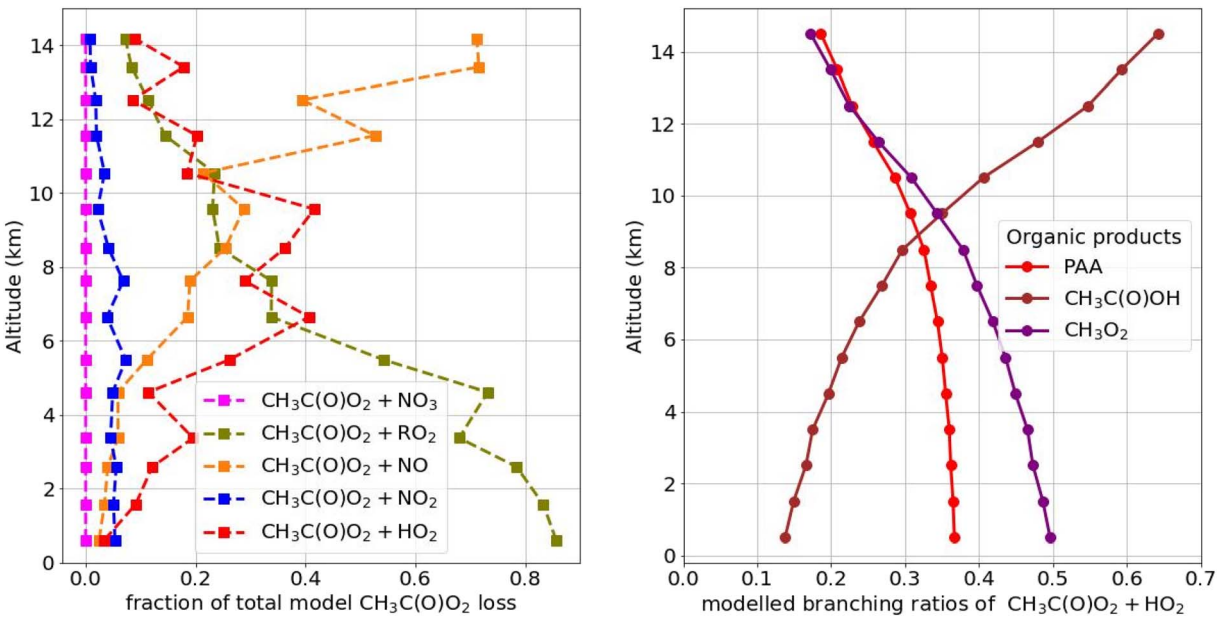

Fig. 8 Modelled median vertical profiles of the fractional loss reactions of $CH_3C(O)O_2$ with NO_3 (pink), RO_2 (olive), NO (orange), NO_2 (blue) and HO_2 (red) of the total modelled $CH_3C(O)O_2$ losses during the CAFE Brazil campaign (left panel). Branching ratios of the reaction of $CH_3C(O)O_2$ with HO_2 leading to the formation of PAA (red), acetic acid ($CH_3C(O)OH$, brown) and CH_3O_2 (purple) based on the latest IUPAC recommendations on the respective rate coefficients (right panel).

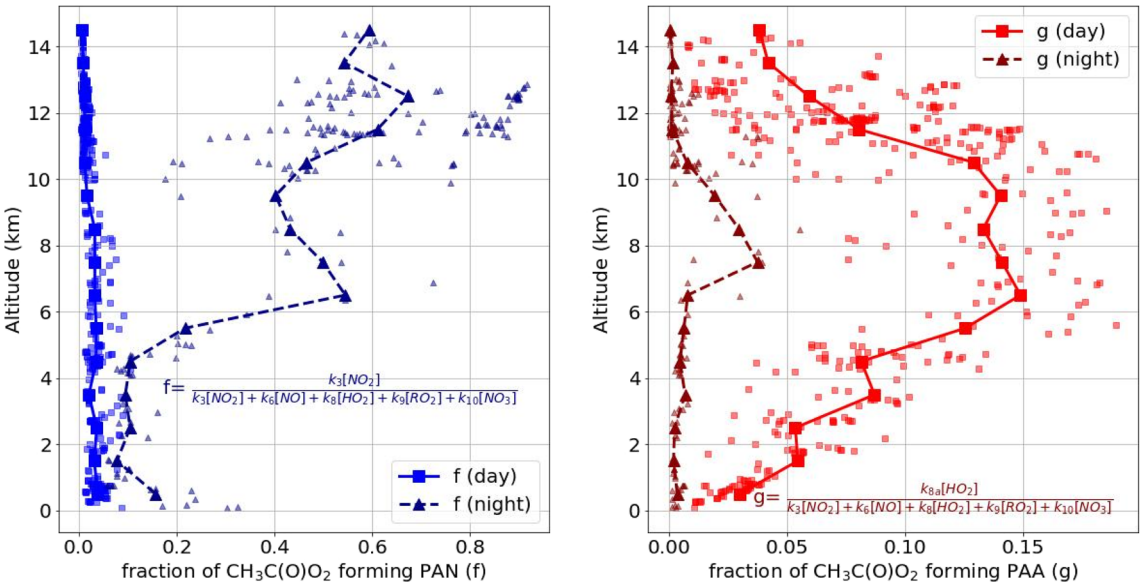

Fig. 9 Median vertical profiles of the fraction of $CH_3C(O)O_2$ forming PAN (*f*, left panel) and PAA (*g*, right panel) based on EMAC model data for CAFE Brazil. Solid lines with squares represent the median of daytime data, where photolysis frequencies of PAN were above 1×10^{-7} s^{-1}, and dashed lines with triangles represent the median of nighttime data, where photolysis frequencies of PAN are zero.

the EMAC simulations along the flight track represents primarily the daytime conditions in the upper troposphere, where the thermal decomposition of PAN is very slow and photolysis frequencies are high.

After identifying the model routes to the production of $CH_3C(O)O_2$, we now analyse its sink terms. The median relative contributions of the modelled loss terms of the $CH_3C(O)O_2$ radical are depicted in Fig. 8. In the upper troposphere above ~10 km, the major loss process for $CH_3C(O)O_2$ is the reaction with NO (R6), which is generated largely by lightning, reducing the concentration of $CH_3C(O)O_2$ available for PAN and PAA formation. The relative contribution of the reaction of $CH_3C(O)O_2$ with HO_2 peaks in the mid altitude-range, and the reactions with RO_2 (the sum of all organic peroxy radicals) species make up the dominant fraction at altitudes below 6 km. Fig. 8 also shows that, on average, only a few percent (1–7%) of the $CH_3C(O)O_2$ radical reacts with NO_2 to form PAN. Over the whole vertical profile, the $CH_3C(O)O_2$ + HO_2 reaction (forming PAA and other products; reactions (R8a–c)) exceeds PAN formation up to a factor of 20, underscoring that, in the model, the formation of PAA is favoured over that of PAN. However, only approximately a third of the reaction of $CH_3C(O)O_2$ with HO_2 leads to PAA formation in the mid altitudes (right panel in Fig. 8). As depicted in the right panel of Fig. 8, the reaction of $CH_3C(O)O_2$ with HO_2 mainly leads to the formation of acetic acid ($CH_3C(O)OH$) (reaction (R8b)) at altitudes above 9.5 km and to $CH_3C(O)O$ (reaction (R8c)), which dissociates to form CH_3 (and CO_2) and thus CH_3O_2 (reaction (R7)). The branching ratio (α) of the reaction forming PAA ($\alpha = k_{8a}/(k_{8a} + k_{8b} + k_{8c})$) decreases from 37% at the lowest altitude to 19% at the highest altitude.

Using the modelled loss reactions of $CH_3C(O)O_2$ with NO, NO_2, NO_3, RO_2 and HO_2, we calculated the fraction of $CH_3C(O)O_2$ that reacts to form PAN (defined as *f* in eqn (1)) and the fraction that reacts to form PAA (defined as *g* in eqn (2)). The median vertical profiles of *f* and *g* for all flights during the day (squares) and during the night (triangles) are depicted in Fig. 9. Nighttime is defined when photolysis frequencies of PAN and acetone were equal to zero, and daytime when photolysis frequencies of PAN and acetone were above 1×10^{-7} s^{-1}. The medians of 1 km vertical bins is given by the solid (day) and dashed (night) lines.

As seen in Fig. 9 (left panel), the fraction *f* of the $CH_3C(O)O_2$ radicals forming PAN during CAFE Brazil is very low (median <0.04) during the day, with the largest values at lower altitudes. The decrease in *f* with altitude (<0.01 at the highest altitudes) is mainly due to the reaction of $CH_3C(O)O_2$ with NO. During the night, NO is converted to NO_2, and hence median PAN formation can reach up to 70% of the total $CH_3C(O)O_2$ losses at 13 km altitude. However, the high value of *f* during the night in the middle and upper troposphere does not lead to a significant accumulation of PAN because of the low concentration of $CH_3C(O)O_2$, which is around two to three orders of magnitude lower at night than during the day at these altitudes. Therefore, the absolute production rate of PAN at 8–14 km altitude is 16–250 times lower during the night than during the day.

As seen in the left panel of Fig. 8, at low altitudes, reaction with RO_2 is the dominant sink for $CH_3C(O)O_2$, which is true during both day and night. During the night, 12% of $CH_3C(O)O_2$ reacts to form PAN at the lowest altitude. However, as PAN is thermally unstable at these altitudes, even large values of *f* do not lead to a significant increase in the PAN concentration.

During the day, the median fraction *g* of the $CH_3C(O)O_2$ radical forming PAA increases steeply from around 0.03 in the boundary layer up to 0.15 in the mid troposphere. Above 9 km altitude, *g* decreases again to 0.04 in the UT. In the middle

troposphere, the daytime maximum in g results from the dominance of the reaction of $CH_3C(O)O_2$ with RO_2 at the lower altitudes and with NO in the UT. In addition, the calculated decrease in g at high altitudes results from a decrease in the branching ratio to PAA in the reaction of $CH_3C(O)O_2$ with HO_2. During the night, PAA formation is negligible (g < 0.01) at almost all altitudes.

The ratio (g/f) is equivalent to $\alpha\ k_8[HO_2]/k_3[NO_2]$[9] and has a value of ~10 at 10 km during the day, corresponding to a factor 5 more HO_2 than NO_2 above the Amazon rainforest at this altitude (see Fig. S7 in the SI).

The low values of both f and g (<0.04) during the day in the UT make prediction of PAN and PAA mixing ratios challenging for global models, as uncertainty in the NO, NO_2, HO_2 and RO_2 mixing ratios has a large impact on PAN and PAA formation. This underlines the importance of an accurate model representation of these species, notably NO (the major reaction partner for $CH_3C(O)O_2$ in the UT), for a correct simulation of PAN and PAA. Below, we examine the repercussions of the inefficient conversion of $CH_3C(O)O_2$ to PAN on the formation of CH_3O_2 and CH_3OOH, which are products of the reactions of $CH_3C(O)O_2$ with HO_2, RO_2 and NO.

4.3 Impact of $CH_3C(O)O_2$ chemistry on CH_3O_2 and CH_3OOH

As shown above, our model results indicate that the photooxidation of isoprene leads to a high rate of production of $CH_3C(O)O_2$ radicals over the Amazon rainforest and that only a small fraction of $CH_3C(O)O_2$ reacts to form PAN or PAA. The largest fraction of $CH_3C(O)O_2$ reacts with one of NO, RO_2 or HO_2 ((R6), (R9), and (R8)) to form acetic acid and the methylperoxy radical, CH_3O_2 (see Fig. 1). The fate of the methylperoxy radical is reaction with NO (R18), NO_2 (R19), HO_2 (R20) and other RO_2 (R21), ultimately leading to the formation of methylperoxynitrate ($CH_3O_2NO_2$, MPN), methylhydroperoxide (CH_3OOH, MHP) and formaldehyde (HCHO) (R22):

$$CH_3O_2 + NO \rightarrow CH_3O + NO_2 \quad (R18)$$

$$CH_3O_2 + NO_2 + M \rightarrow CH_3O_2NO_2 + M \quad (R19)$$

$$CH_3O_2 + HO_2 \rightarrow CH_3OOH + O_2 \quad (R20)$$

$$CH_3O_2 + RO_2 \rightarrow CH_3O + RO + O_2 \quad (R21)$$

$$CH_3O + O_2 \rightarrow HCHO + HO_2 \quad (R22)$$

CH_3OOH is one of the most abundant hydroperoxides in the atmosphere, while $CH_3O_2NO_2$ can be an important reservoir of NO_X at high altitudes where it is thermally stable.[57] HCHO is a central source of HO_x radicals at all altitudes[58] and has been used to indirectly estimate surface isoprene emissions[59,60] (Millet *et al.*, 2006; Mahajan *et al.*, 2011).

All these C_1 trace gases are generally recognized as resulting from the OH-initiated oxidation of methane. Here, we examine the vertically resolved contributions of methane and isoprene oxidation to the formation of CH_3O_2 and thus CH_3OOH, $CH_3O_2NO_2$ and HCHO over the Amazon rainforest.

Fig. 10 compares the modelled absolute and relative production rates of CH_3O_2 from the reactions of $CH_3C(O)O_2$ with NO, RO_2, and NO_3, and from the OH-initiated oxidation of methane. As seen in Fig. 10 (left panel), the median total production of CH_3O_2 in the model ranges from 0.16 pptv s^{-1} in the boundary layer down to around 0.01 pptv s^{-1} in the UT. The CH_3O_2 production from the OH-initiated oxidation of methane has a maximum at about 4 km altitude (0.05 pptv s^{-1}), while the maximum median production from $CH_3C(O)O_2$ is in the lowest altitude bin, with around 0.06 ppvt s^{-1}.

As depicted in Fig. 10 (right panel), the reactions of OH with methane and $CH_3C(O)O_2$ with NO, RO_2 and HO_2 together contribute approximately 60% of the total CH_3O_2 production in the model (grey dashed line). The other 40% arise from *e.g.* CH_3 radical generation *via* acetone photolysis and the further photochemical degradation of isoprene products. The

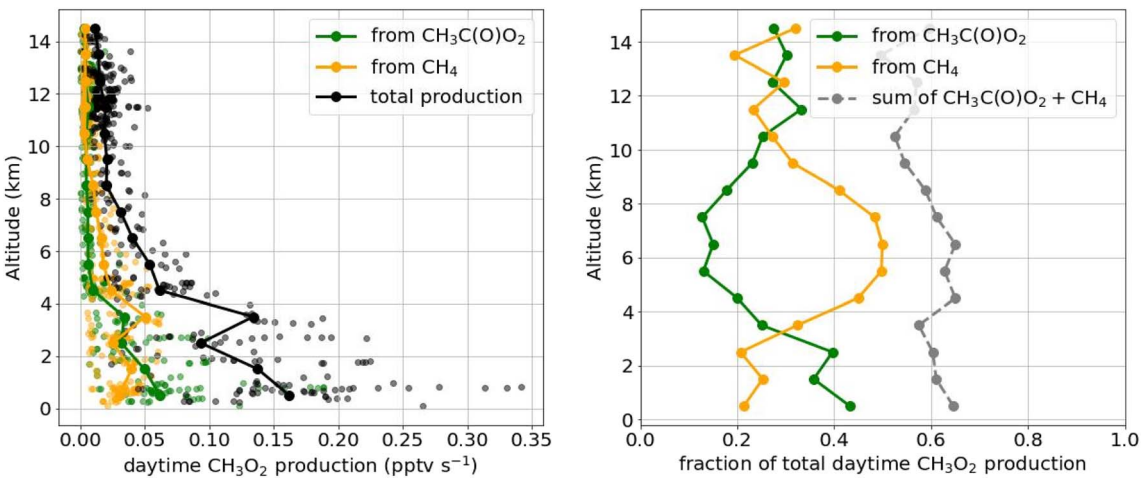

Fig. 10 Median vertical profiles of calculated methyl peroxy radical (CH_3O_2) production rates *via* the reactions of $CH_3C(O)O_2$ with NO, RO_2 and HO_2 (green) and OH + methane (orange) based on EMAC model results for the CAFE Brazil campaign (left panel). Median relative contribution of $CH_3C(O)O_2$ (green) and OH + methane (orange) to the total CH_3O_2 production in the model and the summed contribution of both terms (grey) (right panel).

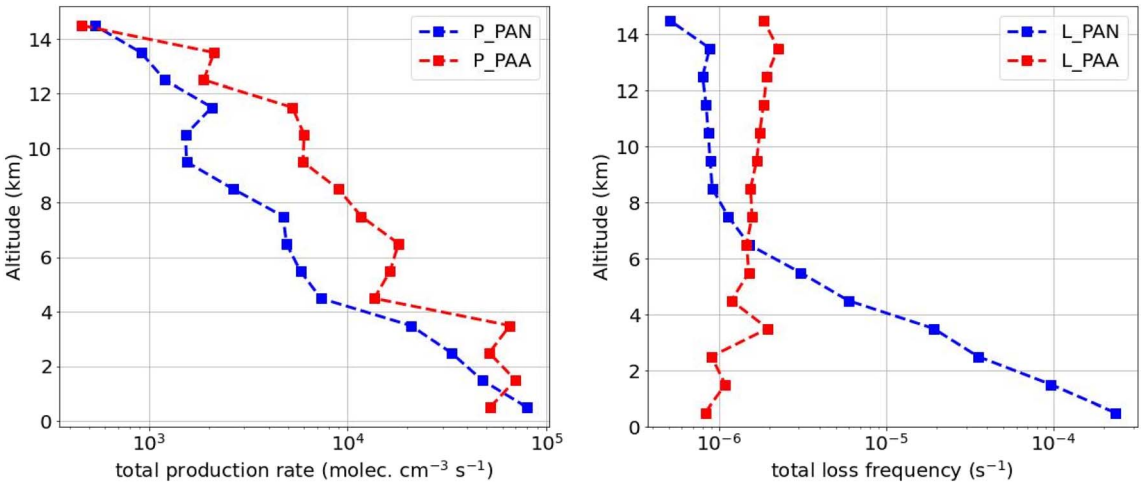

Fig. 11 Median total production rate of PAN (blue) and PAA (red) calculated from modelled $CH_3C(O)O_2$ concentrations (left panel). Median total loss rate of PAN (blue) and PAA (red) calculated from modelled photolysis frequencies and reaction with OH (right panel).

production of CH_3O_2 from $CH_3C(O)O_2$ is most important at low altitudes, where the reaction with RO_2 is dominant, accounting for around 43%. In the UT above ~10 km, the contributions of CH_4 and $CH_3C(O)O_2$ are both around 30% and hence equally important for the production of CH_3OOH, CH_3OONO_2 and HCHO over the Amazon rainforest.

4.4 Role of *in situ* chemistry and transport for PAN and PAA during CAFE Brazil

Here, based on model results, we examine to what extent *in situ* chemical production and loss or transport are the main factors controlling the abundance and vertical distribution of both trace gases. To do this, we derive the instantaneous chemical production rate of PAN and PAA (P_PAN and P_PAA) based on modelled concentrations of $CH_3C(O)O_2$ and its reaction partners as follows:

$$\text{P\_PAN} = k_3[CH_3C(O)O_2][NO_2] \quad (3)$$

$$\text{P\_PAA} = k_{8a}[CH_3C(O)O_2][HO_2] \quad (4)$$

The instantaneous loss frequencies (L_PAN and L_PAA in s^{-1}) are given by:

$$\text{L\_PAN} = J_{5b} + (J_{5a} + k_4)(1 - f) \quad (5)$$

$$\text{L\_PAA} = J_{11} + k_{12}[OH] \quad (6)$$

In these expressions, J_i represents the photolysis frequency associated with reaction R_i.

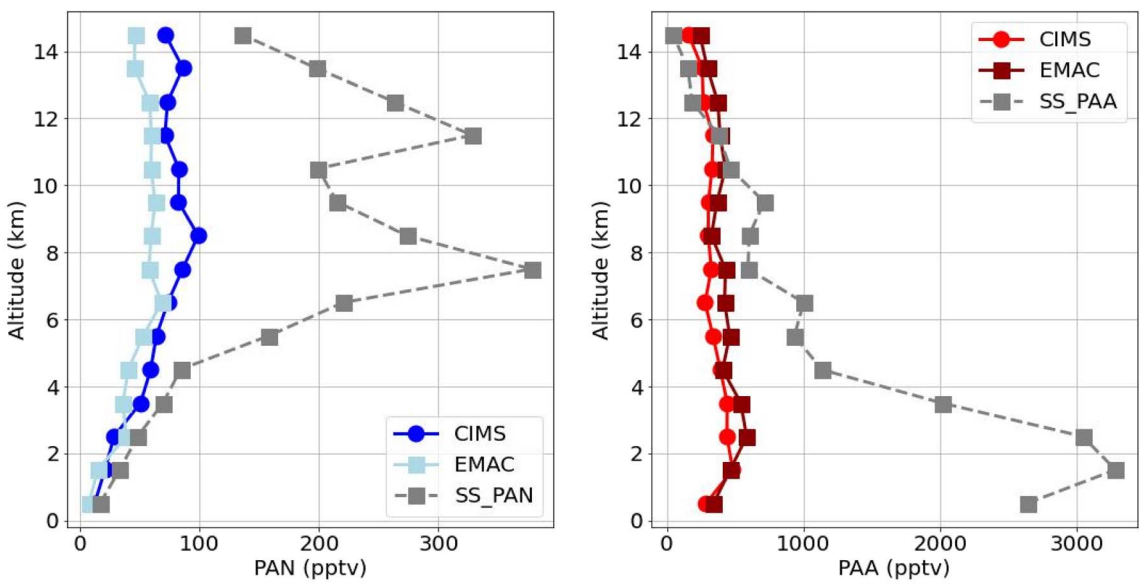

Fig. 12 Median vertical profiles of measured (solid line with circles), modelled (solid line with squares) and calculated "steady state" concentrations (grey dashed line with squares) for PAN (left panel) and PAA (right panel) during CAFE Brazil.

Using expressions (3–6), and concentrations of $CH_3C(O)O_2$, NO, NO_2, HO_2 and RO_2 from the EMAC model output (7.5 min time steps along the flight tracks), we can calculate *in situ* production and loss terms for both PAN and PAA and their dependence on altitude. The median daytime and nighttime vertical profiles of modelled NO_X, HO_X and $CH_3C(O)O_2$ mixing ratios are depicted in Fig. S7 in the SI.

Fig. 11 shows the results for daytime production and loss rates. As shown in Fig. S6 in the SI, the loss rate of PAN is dominated by thermal decomposition up to 6 km altitude, after which photolysis becomes the dominant term. The PAA losses due to reaction with OH are slower (by up to a factor of 20) than those due to photolysis during the day and are hence almost negligible.

Ignoring the role of transport and assuming the chemical system is in steady-state, the mixing ratios of PAN and PAA can be calculated from the ratio of production and loss terms, *i.e.* SS_PAN = P_PAN/L_PAN and SS_PAA = P_PAA/L_PAA. The results are displayed as median vertical profiles (using data from all flights where PAN and PAA were measured) in Fig. 12, which compares "steady state" PAN and PAA mixing ratios calculated from model reactant concentrations, rate coefficients and photolysis frequencies with those output by the model for each time step. The calculated steady-state PAN mixing ratios (grey dashed line in the left panel of Fig. 12) are up to a factor of 6.5 higher than modelled median PAN (light blue) in the mid and upper altitudes, whereas the calculated steady-state concentration of PAA exceeds the modelled median by almost a factor of 8 in low altitudes <3 km, indicating that the chemical steady-state assumption may not be applicable for PAN and PAA under the conditions during CAFE Brazil. This relates to the timescales required to establish a steady state compared to those for vertical mixing.

Based on EMAC vertical updraft velocities, air parcels are estimated to rise to an altitude of 6 km within around 3–4 min. The time it takes to establish a steady state can be approximated by the loss rate constant and the first-order production rate. In the case of PAN, the time (τ_{ss}) required to establish steady state depends on the rates of the forward reaction (R3) and reverse reactions (*e.g.* (R4)). Rate coefficients, retrieved from the model, at 6 km altitudes are around 1.0×10^{-11} cm^3 molecule^{-1} s^{-1} for k_3 and 8×10^{-7} s^{-1} for k_4. With typical NO_2 concentrations of around 1.2×10^8 molecule cm^{-3} at this altitude, this results in an approximate time to establish a steady state of >20 min.

Hence, vertical mixing due to convection can be much faster than *in situ* production at mid-tropospheric altitudes during CAFE Brazil. Rapidly upward-moving air masses from the boundary layer, where almost no PAN is present, would lead to a dilution of PAN-rich layers in the mid and upper troposphere. In contrast, the lifetime of PAA in the boundary layer due to photolysis is almost two weeks (see Fig. S8 in the SI). Therefore, the vertical transport of PAA-rich air from the boundary layer would lead to an increase in PAA levels in the mid and upper troposphere.

Since EMAC-modelled PAN and PAA are in good agreement with the observations, we conclude that the vertical profiles of PAN and PAA during CAFE Brazil are strongly influenced by vertical mixing and altitude-dependent chemistry along back-trajectories rather than *in situ* chemistry in the UT. In the absence of accurate, altitude dependent HO_2 and RO_2 measurements required to validate the model concentrations of these radicals, we cannot, however, rule out that the good agreement between the model and measurement partially reflects cancellation of errors in both the chemical production and loss terms of PAN and transport.

5 Conclusions

A unique dataset of simultaneous airborne CIMS measurements of PAN and PAA in an altitude range from 0.3–15 km over the Amazon rainforest has been used to evaluate the production and losses of the precursor $CH_3C(O)O_2$ radical with the help of the global chemical transport model EMAC.

Generally, PAA mixing ratios exceeded observed PAN levels by up to a factor of 5 in the mid troposphere, underlining the dominance of HO_2 over NO_2 chemistry in the pristine, natural environment under low NO_X conditions of the Amazon rainforest. The mixing ratios of PAN and PAA during the CAFE Brazil aircraft campaign over the Amazon rainforest were well represented by the EMAC model within the measurement uncertainties. The tendency of the model to overestimate the PAA/PAN ratio may indicate a positive bias in the HO_2-to-NO_2 ratio.

The analysis of model production terms for the common PAN and PAA precursor radical, $CH_3C(O)O_2$, revealed that $CH_3C(O)O_2$ formation over the Amazon rainforest is primarily (>50%) driven by isoprene and its photooxidation products. Only around 8% of the $CH_3C(O)O_2$ radicals in the model was recycled *via* thermal dissociation of PAN; the vast majority was produced primarily *via* photochemical formation of CH_3CO. The most important single contribution to the total modelled CH_3CO production during CAFE Brazil was the isoprene oxidation product methylglyoxal ($CH_3C(O)CHO$), which contributed more than 30% *via* photolysis (25.3%) and the reaction with OH (5.8%). The second and third most important precursors of CH_3CO were acetaldehyde (*ca.* 17%), which may also partly originate from biogenic VOC emissions of the rainforest, and methyl vinyl ketone (*ca.* 10%), another isoprene oxidation product. The contribution of acetone and its oxidation products to the modelled CH_3CO production totalled ~14%, which can be a result of both anthropogenic and biogenic emissions.

The fraction of $CH_3C(O)O_2$ radicals that react with NO_2, forming PAN (f), or with HO_2, forming PAA (g), was very low (<4% during daytime in the UT). The major loss reaction for $CH_3C(O)O_2$ in the UT is its reaction with NO, while at low altitudes, the reaction with RO_2 is dominant. Both reactions lead to the formation of acetic acid and the methyl peroxy radical CH_3O_2, which is a precursor of methylperoxy nitrate ($CH_3O_2NO_2$), methylhydroperoxide (CH_3OOH) and formaldehyde (HCHO). We showed that CH_3O_2 production from $CH_3C(O)O_2$ chemistry competes with that from methane oxidation in the UT and even exceeds methane-driven CH_3O_2 production at altitudes below 4 km, further underlining the

importance of isoprene emissions on photochemical processes over the Amazon rainforest.

By calculating a chemical steady-state based on the model $CH_3C(O)O_2$, HO_2, and NO_X concentrations, it became evident that the vertical profile of PAN and PAA during CAFE Brazil was significantly influenced by vertical mixing and photochemistry along the back trajectories, which circulated above the South American continent in the mid and upper troposphere at least 10 days before sampling.

Author contributions

Conceptualization: JL, JC, and AP. Formal analysis: CN and JC. Funding acquisition: JL. Investigation-field work: CN, RD, and SA. Investigation-model simulations: MK, SG, and AP. Writing (original draft): CN. Writing (review and editing): JC and all authors.

Conflicts of interest

There are no conflicts to declare.

Data availability

Measurement and model data for this article (time series in ASCII format) are available at the Max-Planck repository [EDMOND] at https://doi.org/10.17617/3.VBUKAV.

Supplementary information (SI) is available. See DOI: https://doi.org/10.1039/d5ea00169b.

Acknowledgements

We thank the HALO pilots and ground crew for their indispensable participation in the CAFE Brazil mission.

References

1 J. E. Lovelock, PAN in the Natural Environment; Its Possible Significance in the Epidemiology of Skin Cancer, *Ambio*, 1977, **6**, 131–133.
2 H. B. Singh, Reactive nitrogen in the troposphere, *Env. Sci. Tech.*, 1987, **21**, 320–327.
3 H. B. Singh and P. L. Hanst, Peroxyacetyl nitrate (PAN) in the unpolluted atmosphere: An important reservoir for nitrogen oxides, *Geophys. Res. Lett.*, 1981, **8**, 941–944.
4 B. J. Finlayson-Pitts and J. N. Pitts, Tropospheric Air Pollution: Ozone, Airborne Toxics, Polycyclic Aromatic Hydrocarbons, and Particles, *Science*, 1997, **276**, 1045–1051.
5 B. J. Finlayson-Pitts and J. N. Pitts, *Chemistry of the Upper and Lower Atmosphere*, Academic Press, San Diego, 2000.
6 J. N. Crowley, N. Pouvesle, G. J. Phillips, R. Axinte, H. Fischer, T. Petäjä, A. Nölscher, J. Williams, K. Hens, H. Harder, M. Martinez-Harder, A. Novelli, D. Kubistin, B. Bohn and J. Lelieveld, Insights into HOx and ROx chemistry in the boreal forest via measurement of peroxyacetic acid, peroxyacetic nitric anhydride (PAN) and hydrogen peroxide, *Atmos. Chem. Phys.*, 2018, **18**, 13457–13479.
7 G. J. Phillips, N. Pouvesle, J. Thieser, G. Schuster, R. Axinte, H. Fischer, J. Williams, J. Lelieveld and J. N. Crowley, Peroxyacetyl nitrate (PAN) and peroxyacetic acid (PAA) measurements by iodide chemical ionisation mass spectrometry: first analysis of results in the boreal forest and implications for the measurement of PAN fluxes, *Atmos. Chem. Phys.*, 2013, **13**, 1129–1139.
8 X. Zhang, Z. M. Chen, S. Z. He, W. Hua, Y. Zhao and J. L. Li, Peroxyacetic acid in urban and rural atmosphere: concentration, feedback on PAN-NO(x) cycle and implication on radical chemistry, *Atmos. Chem. Phys.*, 2010, **10**, 737–748.
9 J. N. Crowley, R. Dörich, P. Eger, F. Helleis, I. Tadic, H. Fischer, J. Williams, A. Edtbauer, N. Wang, B. A. Holanda, M. Poehlker, U. Pöschl, A. Pozzer and J. Lelieveld, Peroxy acetyl nitric anhydride (PAN) and peroxy acetic acid (PAA) over the Atlantic west of Africa during CAFE-Africa and the influence of biomass-burning, *Environ. Sci.: Atmos.*, 2025, **5**, 620–635.
10 K. R. Travis, C. L. Heald, H. M. Allen, E. C. Apel, S. R. Arnold, D. R. Blake, W. H. Brune, X. Chen, R. Commane, J. D. Crounse, B. C. Daube, G. S. Diskin, J. W. Elkins, M. J. Evans, S. R. Hall, E. J. Hintsa, R. S. Hornbrook, P. S. Kasibhatla, M. J. Kim, G. Luo, K. McKain, D. B. Millet, F. L. Moore, J. Peischl, T. B. Ryerson, T. Sherwen, A. B. Thames, K. Ullmann, X. Wang, P. O. Wennberg, G. M. Wolfe and F. Yu, Constraining remote oxidation capacity with ATom observations, *Atmos. Chem. Phys.*, 2020, **20**, 7753–7781.
11 J. D. Crounse, K. A. McKinney, A. J. Kwan and P. O. Wennberg, Measurement of gas-phase hydroperoxides by chemical ionization mass spectrometry, *Anal. Chem.*, 2006, **78**, 6726–6732.
12 J. A. Lind, A. L. Lazrus and G. L. Kok, Aqueous phase oxidation of sulfur(IV) by hydrogen peroxide, methylhydroperoxide, and peroxyacetic acid, *J. Geophys. Res. Atmos.*, 1987, **92**, 4171–4177.
13 A. R. Baker, M. Kanakidou, A. Nenes, S. Myriokefalitakis, P. L. Croot, R. A. Duce, Y. Gao, C. Guieu, A. Ito, T. D. Jickells, N. M. Mahowald, R. Middag, M. M. G. Perron, M. M. Sarin, R. Shelley and D. R. Turner, Changing atmospheric acidity as a modulator of nutrient deposition and ocean biogeochemistry, *Sci. Adv.*, 2021, **7**, eabd8800.
14 B. J. Finlayson-Pitts and J. N. Pitts, in *Chemistry of the Upper and Lower Atmosphere*, eds. B. J. Finlayson-Pitts and J. N. Pitts, Academic Press, San Diego, 2000, pp. 264–293, DOI: 10.1016/B978-012257060-5/50009-5.
15 A. Guenther, Biological and chemical diversity of biogenic volatile organic emissions into the atmosphere, *Int. Sch. Res. Not.*, 2013, **2013**, 786290.
16 J. M. Roberts, in *Volatile Organic Compounds in the Atmosphere*, Blackwell Publishing Ltd, Oxford, U.K., 2007, pp. 221–268.
17 H. B. Singh, D. Herlth, D. O'Hara, L. Salas, A. L. Torres, G. L. Gregory, G. W. Sachse and J. F. Kasting, Atmospheric peroxyacetyl nitrate measurements over the Brazilian

Amazon Basin during the wet season: Relationships with nitrogen oxides and ozone, *J. Geophys. Res. Atmos.*, 1990, **95**, 16945–16954.

18 H. B. Singh, D. Herlth, R. Kolyer, R. Chatfield, W. Viezee, L. J. Salas, Y. Chen, J. D. Bradshaw, S. T. Sandholm, R. Talbot, G. L. Gregory, B. Anderson, G. W. Sachse, E. Browell, A. S. Bachmeier, D. R. Blake, B. Heikes, D. Jacob and H. E. Fuelberg, Impact of biomass burning emissions on the composition of the South Atlantic troposphere: Reactive nitrogen and ozone, *J. Geophys. Res. Atmos.*, 1996, **101**, 24203–24219.

19 C. Keim, G. Y. Liu, C. E. Blom, H. Fischer, T. Gulde, M. Höpfner, C. Piesch, F. Ravegnani, A. Roiger, H. Schlager and N. Sitnikov, Vertical profile of peroxyacetyl nitrate (PAN) from MIPAS-STR measurements over Brazil in February 2005 and its contribution to tropical UT NO_y partitioning, *Atmos. Chem. Phys.*, 2008, **8**, 4891–4902.

20 M. A. Franco, L. V. Rizzo, M. J. Teixeira, P. Artaxo, T. Azevedo, J. Lelieveld, C. A. Nobre, C. Pöhlker, U. Pöschl, J. Shimbo, X. Xu and L. A. T. Machado, How climate change and deforestation interact in the transformation of the Amazon rainforest, *Nat. Commun.*, 2025, **16**, 7944.

21 Y. Malhi and O. Phillips, *Tropical Forests and Global Atmospheric Change*, Oxford University Press, Oxford, 2005.

22 E. V. Fischer, D. J. Jacob, R. M. Yantosca, M. P. Sulprizio, D. B. Millet, J. Mao, F. Paulot, H. B. Singh, A. Roiger, L. Ries, R. W. Talbot, K. Dzepina and S. P. Deolal, Atmospheric peroxyacetyl nitrate (PAN): a global budget and source attribution, *Atmos. Chem. Phys.*, 2014, **14**, 2679–2698.

23 C. B. M. Groß, T. J. Dillon and J. N. Crowley, Pressure dependent OH yields in the reactions of CH_3CO and $HOCH_2CO$ with O_2, *Phys. Chem. Chem. Phys.*, 2014, **16**, 10990–10998.

24 G. Kovacs, J. Zador, E. Farkas, R. Nadasdi, I. Szilagyi, S. Dobe, T. Berces, F. Marta and G. Lendvay, Kinetics and mechanism of the reactions of CH3CO and CH3C(O)CH2 radicals with O2. Low-pressure discharge flow experiments and quantum chemical computations, *Phys. Chem. Chem. Phys.*, 2007, **9**, 4142–4154.

25 M. Ammann, R. A. Cox, J. N. Crowley, H. Herrmann, M. E. Jenkin, V. F. McNeill, A. Mellouki, M. J. Rossi, J. Troe and T. J. Wallington, *IUPAC Task Group on Atmospheric Chemical Kinetic Data Evaluation*, 2025, https://iupac.aeris-data.fr/.

26 M. Berasategui, D. Amedro, L. Vereecken, J. Lelieveld and J. N. Crowley, Reaction between $CH_3C(O)OOH$ (peracetic acid) and OH in the gas phase: a combined experimental and theoretical study of the kinetics and mechanism, *Atmos. Chem. Phys.*, 2020, **20**, 13541–13555.

27 R. Atkinson, D. L. Baulch, R. A. Cox, J. N. Crowley, R. F. Hampson, R. G. Hynes, M. E. Jenkin, M. J. Rossi and J. Troe, Evaluated kinetic and photochemical data for atmospheric chemistry: Volume II - reactions of organic species, *Atmos. Chem. Phys.*, 2006, 3625–4055, DOI: 10.5194/acp-6-3625-2006.

28 J. N. Crowley, R. Dörich, P. Eger, F. Helleis, I. Tadic, H. Fischer, J. Williams, A. Edtbauer, N. Wang, B. A. Holanda, M. Poehlker, U. Pöschl, A. Pozzer and J. Lelieveld, Peroxy acetyl nitric anhydride (PAN) and peroxy acetic acid (PAA) over the Atlantic west of Africa during CAFE-Africa and the influence of biomass-burning, *Environ. Sci.: Atmos.*, 2025, **5**, 620–635.

29 J. Curtius, M. Heinritzi, L. J. Beck, M. L. Pöhlker, N. Tripathi, B. E. Krumm, P. Holzbeck, C. M. Nussbaumer, L. Hernández Pardo, T. Klimach, K. Barmpounis, S. T. Andersen, R. Bardakov, B. Bohn, M. A. Cecchini, J.-P. Chaboureau, T. Dauhut, D. Dienhart, R. Dörich, A. Edtbauer, A. Giez, A. Hartmann, B. A. Holanda, P. Joppe, K. Kaiser, T. Keber, H. Klebach, O. O. Krüger, A. Kürten, C. Mallaun, D. Marno, M. Martinez, C. Monteiro, C. Nelson, L. Ort, S. S. Raj, S. Richter, A. Ringsdorf, F. Rocha, M. Simon, S. Sreekumar, A. Tsokankunku, G. R. Unfer, I. D. Valenti, N. Wang, A. Zahn, M. Zauner-Wieczorek, R. I. Albrecht, M. O. Andreae, P. Artaxo, J. N. Crowley, H. Fischer, H. Harder, D. L. Herdies, L. A. T. Machado, C. Pöhlker, U. Pöschl, A. Possner, A. Pozzer, J. Schneider, J. Williams and J. Lelieveld, Isoprene nitrates drive new particle formation in Amazon's upper troposphere, *Nature*, 2024, **636**, 124–130.

30 A. Giez, M. Zöger, C. Mallaun, V. Nenakhov, M. Schimpf, C. Grad, A. Numbeger and K. Raynor, *Determination of the Measurement Errors for the HALO Basic Data System Bahamas by Means of Error Propagation*, Forschungsbericht ISSN, Köln, 2022, pp. 1434–8454.

31 A. F. Stein, R. R. Draxler, G. D. Rolph, B. J. B. Stunder, M. D. Cohen and F. Ngan, NOAA'S HYSPLIT atmospheric transport and dispersion modeling system, *Bull. Am. Met. Soc.*, 2015, **96**, 2059–2077.

32 C. Voigt, J. Lelieveld, H. Schlager, J. Schneider, J. Curtius, R. Meerkötter, D. Sauer, L. Bugliaro, B. Bohn, J. N. Crowley, T. Erbertseder, S. Groß, V. Hahn, Q. Li, M. Mertens, M. L. Pöhlker, A. Pozzer, U. Schumann, L. Tomsche, J. Williams, A. Zahn, M. Andreae, S. Borrmann, T. Bräuer, R. Dörich, A. Dörnbrack, A. Edtbauer, L. Ernle, H. Fischer, A. Giez, M. Granzin, V. Grewe, H. Harder, M. Heinritzi, B. A. Holanda, P. Jöckel, K. Kaiser, O. O. Krüger, J. Lucke, A. Marsing, A. Martin, S. Matthes, C. Pöhlker, U. Pöschl, S. Reifenberg, A. Ringsdorf, M. Scheibe, I. Tadic, M. Zauner-Wieczorek, R. Henke and M. Rapp, Cleaner skies during the COVID-19 lockdown, *Bull. Am. Met. Soc.*, 2022, E1796–E1827.

33 D. L. Slusher, L. G. Huey, D. J. Tanner, F. M. Flocke and J. M. Roberts, A thermal dissociation-chemical ionization mass spectrometry (TD-CIMS) technique for the simultaneous measurement of peroxyacyl nitrates and dinitrogen pentoxide, *J. Geophys. Res. Atmos.*, 2004, **109**, D19315.

34 W. Zheng, F. M. Flocke, G. S. Tyndall, A. Swanson, J. J. Orlando, J. M. Roberts, L. G. Huey and D. J. Tanner, Characterization of a thermal decomposition chemical ionization mass spectrometer for the measurement of

peroxy acyl nitrates (PANs) in the atmosphere, *Atmos. Chem. Phys.*, 2011, **11**, 6529–6547.

35 R. Dörich, P. Eger, J. Lelieveld and J. N. Crowley, Iodide CIMS and m/z 62: the detection of HNO_3 as NO_3^- in the presence of PAN, peroxyacetic acid and ozone, *Atmos. Meas. Tech.*, 2021, **14**, 5319–5332.

36 P. G. Eger, F. Helleis, G. Schuster, G. J. Phillips, J. Lelieveld and J. N. Crowley, Chemical ionization quadrupole mass spectrometer with an electrical discharge ion source for atmospheric trace gas measurement, *Atmos. Meas. Tech.*, 2019, **12**, 1935–1954.

37 Y. Ji, L. G. Huey, D. J. Tanner, Y. R. Lee, P. R. Veres, J. A. Neuman, Y. Wang and X. Wang, A vacuum ultraviolet ion source (VUV-IS) for iodide–chemical ionization mass spectrometry: a substitute for radioactive ion sources, *Atmos. Meas. Tech.*, 2020, **13**, 3683–3696.

38 P. Warneck and T. Zerbach, Synthesis of peroxyacetyl nitrate in air by acetone photolysis, *Env. Sci. Tech.*, 1992, **26**, 74–79.

39 F. M. Flocke, A. J. Weinheimer, A. L. Swanson, J. M. Roberts, R. Schmitt and S. Shertz, On the measurement of PANs by gas chromatography and electron capture detection, *J. Atmos. Chem.*, 2005, **52**, 19–43.

40 P. Jöckel, H. Tost, A. Pozzer, C. Bruhl, J. Buchholz, L. Ganzeveld, P. Hoor, A. Kerkweg, M. G. Lawrence, R. Sander, B. Steil, G. Stiller, M. Tanarhte, D. Taraborrelli, J. Van Aardenne and J. Lelieveld, The atmospheric chemistry general circulation model ECHAM5/MESSy1: consistent simulation of ozone from the surface to the mesosphere, *Atmos. Chem. Phys.*, 2006, **6**, 5067–5104.

41 P. Jöckel, A. Kerkweg, A. Pozzer, R. Sander, H. Tost, H. Riede, A. Baumgaertner, S. Gromov and B. Kern, Development cycle 2 of the Modular Earth Submodel System (MESSy2), *Geosci. Model Dev.*, 2010, **3**, 717–752.

42 E. Roeckner, G. Bäuml, L. Bonaventura, R. Brokopf, M. Esch, M. Giorgetta, S. Hagemann, I. Kirchner, L. Kornblueh, E. Manzini, S. Hagemann, I. Kirchner, L. Kornblueh, E. Manzini, U. Schlese, U. Schulzweida and A. Tompkins, *The atmospheric general circulation model ECHAM5. PART I: Model description*, Tech. rep., MPI-Report 349, Max Planck Institute for Meteorology, 2003, http://www.mpimet.mpg.de/fileadmin/ publikationen/Reports/max scirep 349.pdf.

43 R. Sander, A. Baumgaertner, D. Cabrera-Perez, F. Frank, S. Gromov, J. U. Grooss, H. Harder, V. Huijnen, P. Jockel, V. A. Karydis, K. E. Niemeyer, A. Pozzer, R. B. Hella, M. G. Schultz, D. Taraborrelli and S. Tauer, The community atmospheric chemistry box model CAABA/MECCA-4.0, *Geosci. Model Dev.*, 2019, **12**, 1365–1385.

44 A. Pozzer, S. F. Reifenberg, V. Kumar, B. Franco, M. Kohl, D. Taraborrelli, S. Gromov, S. Ehrhart, P. Jöckel, R. Sander, V. Fall, S. Rosanka, V. Karydis, D. Akritidis, T. Emmerichs, M. Crippa, D. Guizzardi, J. W. Kaiser, L. Clarisse, A. Kiendler-Scharr, H. Tost and A. Tsimpidi, Simulation of organics in the atmosphere: evaluation of EMACv2.54 with the Mainz Organic Mechanism (MOM) coupled to the ORACLE (v1.0) submodel, *Geosci. Model Dev.*, 2022, **15**, 2673–2710.

45 E. E. McDuffie, S. J. Smith, P. O'Rourke, K. Tibrewal, C. Venkataraman, E. A. Marais, B. Zheng, M. Crippa, M. Brauer and R. V. Martin, A global anthropogenic emission inventory of atmospheric pollutants from sector- and fuel-specific sources (1970–2017): an application of the Community Emissions Data System (CEDS), *Earth Syst. Sci. Data*, 2020, **12**, 3413–3442.

46 M. O. Andreae, Emission of trace gases and aerosols from biomass burning – an updated assessment, *Atmos. Chem. Phys.*, 2019, **19**, 8523–8546.

47 J. W. Kaiser, A. Heil, M. O. Andreae, A. Benedetti, N. Chubarova, L. Jones, J. J. Morcrette, M. Razinger, M. G. Schultz, M. Suttie and G. R. van der Werf, Biomass burning emissions estimated with a global fire assimilation system based on observed fire radiative power, *Biogeosciences*, 2012, **9**, 527–554.

48 A. B. Guenther, X. Jiang, C. L. Heald, T. Sakulyanontvittaya, T. Duhl, L. K. Emmons and X. Wang, The Model of Emissions of Gases and Aerosols from Nature version 2.1 (MEGAN2.1): an extended and updated framework for modeling biogenic emissions, *Geosci. Model Dev.*, 2012, **5**, 1471–1492.

49 V. Grewe, Impact of climate variability on tropospheric ozone, *Sci. Total Environ.*, 2007, **374**, 167–181.

50 P. Jöckel, H. Tost, A. Pozzer, C. Brühl, J. Buchholz, L. Ganzeveld, P. Hoor, A. Kerkweg, M. G. Lawrence, R. Sander, B. Steil, G. Stiller, M. Tanarhte, D. Taraborrelli, J. van Aardenne and J. Lelieveld, The atmospheric chemistry general circulation model ECHAM5/MESSy1: consistent simulation of ozone from the surface to the mesosphere, *Atmos. Chem. Phys.*, 2006, **6**, 5067–5104.

51 C. M. Nussbaumer, M. Kohl, A. Pozzer, I. Tadic, R. Rohloff, D. Marno, H. Harder, H. Ziereis, A. Zahn, F. Obersteiner, A. Hofzumahaus, H. Fuchs, C. Künstler, W. H. Brune, T. B. Ryerson, J. Peischl, C. R. Thompson, I. Bourgeois, J. Lelieveld and H. Fischer, Ozone Formation Sensitivity to Precursors and Lightning in the Tropical Troposphere Based on Airborne Observations, *J. Geophys. Res. Atmos.*, 2024, **129**, e2024JD041168.

52 H. B. Singh, D. O'Hara, D. Herlth, W. Sachse, D. R. Blake, J. D. Bradshaw, M. Kanakidou and P. J. Crutzen, Acetone in the atmosphere: distribution sources and sinks, *J. Geophys. Res. Atmos.*, 1994, **99**, 1805–1819.

53 U. Pöschl, J. Williams, P. Hoor, H. Fischer, P. J. Crutzen, C. Warneke, R. Holzinger, A. Hansel, A. Jordan, W. Lindinger, H. A. Scheeren, W. Peters and J. Lelieveld, High acetone concentrations throughout the 0-12 km altitude range over the tropical rainforest in Surinam, *J. Atmos. Chem.*, 2001, **38**, 115–132.

54 T. M. Fu, D. J. Jacob, F. Wittrock, J. P. Burrows, M. Vrekoussis and D. K. Henze, Global budgets of atmospheric glyoxal and methylglyoxal, and implications for formation of secondary organic aerosols, *J. Geophys. Res. Atmos.*, 2008, **113**, DOI: 10.1029/2007JD009505.

55 E. Gomes Alves, R. Aquino Santana, C. Quaresma Dias-Júnior, S. Botía, T. Taylor, A. M. Yáñez-Serrano, J. Kesselmeier, E. Bourtsoukidis, J. Williams, P. I. Lembo

Silveira de Assis, G. Martins, R. de Souza, S. Duvoisin Júnior, A. Guenther, D. Gu, A. Tsokankunku, M. Sörgel, B. Nelson, D. Pinto, S. Komiya, D. Martins Rosa, B. Weber, C. Barbosa, M. Robin, K. J. Feeley, A. Duque, V. Londoño Lemos, M. P. Contreras, A. Idarraga, N. López, C. Husby, B. Jestrow and I. M. Cely Toro, Intra- and interannual changes in isoprene emission from central Amazonia, *Atmos. Chem. Phys.*, 2023, **23**, 8149–8168.

56 H. Wang, X. Liu, C. Wu and G. Lin, Regional to global distributions, trends, and drivers of biogenic volatile organic compound emission from 2001 to 2020, *Atmos. Chem. Phys.*, 2024, **24**, 3309–3328.

57 B. A. Nault, C. Garland, S. E. Pusede, P. J. Wooldridge, K. Ullmann, S. R. Hall and R. C. Cohen, Measurements of $CH_3O_2NO_2$ in the upper troposphere, *Atmos. Meas. Tech.*, 2015, **8**, 987–997.

58 L. Jaeglé, D. J. Jacob, P. O. Wennberg, C. M. Spivakovsky, T. F. Hanisco, E. J. Lanzendorf, E. J. Hintsa, D. W. Fahey, E. R. Keim, M. H. Proffitt, E. L. Atlas, F. Flocke, S. Schauffler, C. T. McElroy, C. Midwinter, L. Pfister and J. C. Wilson, Observed OH and HO_2 in the upper troposphere suggest a major source from convective injection of peroxides, *Geophys. Res. Lett.*, 1997, **24**, 3181–3184.

59 D. B. Millet, D. J. Jacob, S. Turquety, R. C. Hudman, S. Wu, A. Fried, J. Walega, B. G. Heikes, D. R. Blake, H. B. Singh, B. E. Anderson and A. D. Clarke, Formaldehyde distribution over North America: Implications for satellite retrievals of formaldehyde columns and isoprene emission, *J. Geophys. Res. Atmos.*, 2006, 111.

60 A. S. Mahajan, L. K. Whalley, E. Kozlova, H. Oetjen, L. Mendez, K. L. Furneaux, A. Goddard, D. E. Heard, J. M. C. Plane and A. Saiz-Lopez, DOAS observations of formaldehyde and its impact on the HOx balance in the tropical Atlantic marine boundary layer, *J. Atmos. Chem.*, 2010, **66**, 167–178.

